

***Final Draft***  
of the original manuscript:

Kupka, D.; Huber, N.; Lilleodden, E.T.:

**A combined experimental-numerical approach for elasto-plastic fracture of individual grain boundaries**

In: Journal of the Mechanics and Physics of Solids (2013) Elsevier

DOI: 10.1016/j.jmps.2013.12.004

# A combined experimental-numerical approach for elasto-plastic fracture of individual grain boundaries

D. Kupka\*, N. Huber, E. T. Lilleodden

*Institute of Materials Research, Materials Mechanics, Helmholtz-Zentrum Geesthacht,  
Max-Planck-Strasse 1, D-21502 Geesthacht, Germany*

---

## Abstract

The parameters for a crystal plasticity finite element constitutive law were calibrated for the aluminum-lithium alloy 2198 using micro-column compression testing on single crystalline volumes. The calibrated material model was applied to simulations of micro-cantilever deflection tests designed for micro-fracture experiments on single grain boundaries. It was shown that the load-displacement response and the local deformation of the grains, which was measured by digital image correlation, were predicted by the simulations. The fracture properties of individual grain boundaries were then determined in terms of a traction-separation-law associated with a cohesive zone. This combination of experiments and crystal plasticity finite element simulations allows the investigation of the fracture behavior of individual grain boundaries in plastically deforming metals.

*Keywords:* micro-compression, micro-bending, finite element crystal plasticity, intergranular fracture, digital image correlation

---

## 1. Introduction

Methods for investigations into the fracture properties of materials on a microscopic scale based on cantilever bending experiments [1, 2] were recently

---

\*corresponding author

*Email address:* [daniel.kupka@hzg.de](mailto:daniel.kupka@hzg.de) (D. Kupka)

developed in order to gain a better understanding of the resistance of materials against damage and fracture. These experiments were focused on materials which show brittle failure like intermetallic compounds [3, 4], interfaces in nano-components [5] and coatings [1, 6]. Moreover, small-scale experiments were conducted in order to isolate individual grain boundaries in technological materials [7, 8]. These experiments were carried out on materials that showed minor plastic deformation prior to fracture.

In general, plastic deformation limits the applicability of microscopic fracture experiments since the plastic zone in front of a crack tip tends to expand through the complete specimen leading to plastic deformation without fracture. However, plastic deformation prior to fracture was observed in recent microscopic fracture experiments. In a preliminary work, which was carried out on the aluminum lithium alloy 2198, grain boundaries were fractured after plastic deformation of the adjacent grains [9]. This combination of ductile grains and brittle grain boundaries is an important case for ductile technological alloys that show intergranular fracture, e. g. aluminum-lithium alloys [10, 11]. Recent micro-fracture experiments that were conducted on NiAl and tungsten single crystals, respectively, also showed plastic deformation prior to fracture [12, 13] without the presence of a grain boundary. In these cases the anisotropic plastic deformation of the material surrounding the location of fracture must be taken into account for the fracture analysis.

Due to the complex boundary conditions associated with such experiments the analysis of the fracture properties is frequently carried out with the help of finite element simulations. For ductile specimens a suitable description of the plastic deformation is required. In the case of a grain boundary fracture experiments on the microstructural length scale the anisotropic plastic deformation of the grains must be taken into account. Within the framework of continuum mechanics the crystal plasticity finite element method (CPFEM) has evolved as a valuable tool to describe the anisotropic plastic deformation of textured materials and individual grains [14]. For example, Raabe *et al.* [15, 16] used a CPFEM model to predict the deformation of a textured component for a

deep drawing process. Klusemann *et al.* [17] determined the local deformation properties of oligo-crystalline tensile test specimens with the help of a CPFEM model. In these cases the CPFEM model provided a good prediction of the anisotropic plastic deformation of the material.

However, the identification of appropriate material parameters for a CPFEM model is not always straight forward. Especially in the case of technological materials, such as rolled sheets, bulk single crystal data is typically unavailable. One approach to circumvent this problem is to apply the micro-compression test developed by Uchic *et al.* [18]. Such tests have been successfully used to determine the deformation properties on a microscopic scale [19–21]. Raabe *et al.* [22] used a calibrated CPFEM model to investigate the influence of the boundary conditions that are imposed in micro-compression experiments on the deformation behavior of single crystals. They numerically predicted the orientation evolution within micro-compression specimens and they showed the beneficial influence of the indenter to column friction. Furthermore, Soler *et al.* [23] combined micro-compression experiments on single crystalline specimens with the CPFEM to investigate the deformation processes in LiF single crystals. They were able to show that a difference in the flow stress between different types of slip systems leads to an increased sensitivity against misalignments of the micro-column and the compression axis. Another approach for the parameter identification was pursued by Gong *et al.* [24]. They used micro-cantilever bending experiments on titanium single crystals as an experimental base for the parameter identification for a model created by Dunne *et al.* [25] for hcp materials to identify the model parameters. These studies show that micro-mechanical experiments that are preferentially carried out on single crystalline volumes can provide access to the CPFEM parameters.

The purpose of the present work is to incorporate the anisotropic plastic deformation properties in terms of a CPFEM material model into the finite element based fracture analysis of a single grain boundary. While the CPFEM parameters are identified using micro-column compression experiments, the fracture analysis is performed using cohesive zone modeling of the grain boundary,

which allows for a mechanism independent description of the fracture process.

## 2. Experiments

The experiments were conducted on the lithium containing aluminum alloy 2198 in the temper T351. The microstructure of the sheets of AA2198 consists of flat grains elongated in the primary rolling direction (see figure 1). The smallest dimension is the grain thickness, which is nominally  $3\ \mu\text{m}$ . The yield stress and the ultimate tensile stress for the material were determined by macroscopic tensile tests (see table 1). For the simulations an elastic modulus of  $75\ \text{GPa}$  was assumed [26].

state	yield stress ,MPa	UTS ,MPa
T351-L	324	445
T8-L	470	511
T351-T	294	416
T8-T	449	490

Table 1: Yield stress and ultimate tensile stress of the aluminum lithium alloy AA2198 from macroscopic tensile tests

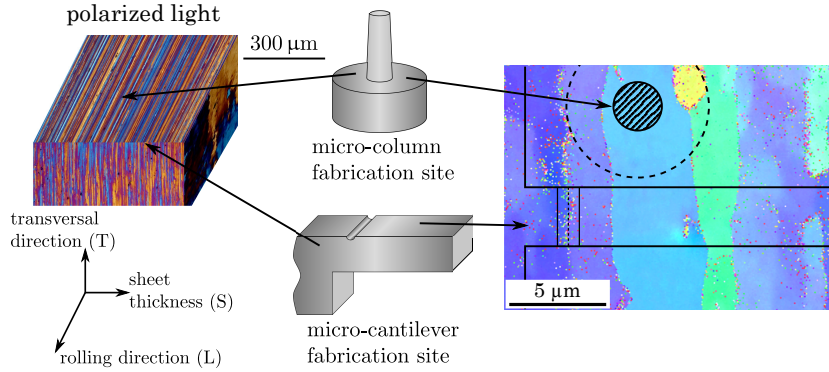


Figure 1: The fabrication sites of the micro-columns and the micro-cantilevers in relation to the microstructure. The image in polarized light was recorded after Barker's etch ( $\text{HBF}_4 + \text{H}_2\text{O}$ , anodized using  $0.2\ \text{A}/\text{cm}^2$ ), the EBSD image was recorded from the polished surface.

Both the cantilevers and the columns were fabricated using focused ion beam (FIB) milling (Nova200, FEI). The cantilevers were fabricated into the edge of the specimen, as given in figure 1. The approximate dimensions of the micro-columns and the micro-cantilevers in relation to the microstructure are also provided in figure 1. The geometry of the micro-cantilevers was adopted from a previous work [9]. A micro-cantilever specimen is shown in figure 2(a). The nominal dimensions of the cantilevers were  $20\ \mu\text{m} : 5\ \mu\text{m} : 8\ \mu\text{m}$  (length : width : height) while the rectangular shape of the cross-section provides a constant crack width during the fracture process. A U-notch was fabricated from the side of the cantilever at the location of the grain boundary close to the supported end to introduce a stress concentration. The well defined notch geometry circumvents any problems associated with the determination of the radius at the notch ground during further analysis. Moreover, the FIB-milling incident to the side of the cantilever prevents uncontrolled implantation of gallium into the material. However, the gallium is expected to additionally embrittle the grain boundary. The orientation of the grains for each cantilever was determined through EBSD-measurements in advance of the fabrication process. The cantilevers were deflected at a prescribed displacement rate of  $5\ \text{nm/s}$  using a nanoindenter (NanoindenterXP, Agilent) equipped with a Berkovich tip. Additionally, cantilevers with the notch placed in a single grain were produced in order to assess the suitability of the micro-compression based identification of CPFEM parameters in absence of a grain boundary under the notch and fracture of the cantilever.

In order to investigate the local deformation behavior, one micro-cantilever bending experiment was conducted *in situ* within the SEM using a nanoindenter (Nanomechanics Inc.) outfitted with a cube-corner tip. The displacement field was measured from the side surface of the cantilever using digital image correlation (DIC) [27, 28]. A speckle pattern was needed to enable the measurement. This pattern was created by depositing Pt-dots combining a gas injection system and the electron beam. Before testing, a reference image of the cantilever was taken. The image of the deformed cantilever was recorded while the load

was held constant. The software for the DIC procedure used within the present study is available at [29].

The parameters of the CPFEM model were calibrated independently from the bending experiments on the basis of compression experiments on single crystalline micro-columns. The micro-columns were fabricated into the polished surface of the sample, normal to the transversal direction (see figure 1). In order to ensure single crystalline volumes, a nominal diameter of 2  $\mu\text{m}$  was chosen. While smaller columns would better ensure single crystalline volumes, size effects may influence deformation properties [19, 30]. Possible size effects for the present material are addressed at the end of section 4. Suitable locations for the column fabrication were identified by EBSD, in order to determine the crystallographic orientation of the column. The columns were fabricated by applying the annular milling technique [19, 31]. The nominal height of the columns was chosen as 6  $\mu\text{m}$  such that an aspect ratio of 1 : 3 (diameter : height) was achieved. This aspect ratio is advantageous since the risk of buckling is minimized while a sufficiently uniaxial stress field is created. A micro-column is shown in figure 2(b). The columns were tested using a nanoindenter (NanoindenterXP, Agilent) equipped with a flat punch tip. The test procedure was displacement controlled by a force feedback loop and the nominal displacement rate,  $\dot{h}$ , was 3 nm/s; resulting in a nominal strain rate of  $0.0005\text{s}^{-1}$ . A tested column is shown in figure 2(c).

### 3. Crystal plasticity model

The crystal plasticity model used in this work is based on the framework of Peirce *et al.* [32] and Asaro [33]. The model is implemented as an ABAQUS user material subroutine (UMAT) based on the work of Huang [34] and later modified by Graff [35]. The anisotropic plastic deformation of a single crystal is captured using a visco-plastic formulation for each slip system in connection with a hardening law. The visco-plasticity is described as:

$$\frac{\dot{\gamma}^\alpha}{\dot{\gamma}_0^\alpha} = \left| \frac{\tau^\alpha}{\tau_Y^\alpha} \right|^n \cdot \text{sign} \left( \frac{\tau^\alpha}{\tau_Y^\alpha} \right), \quad (1)$$

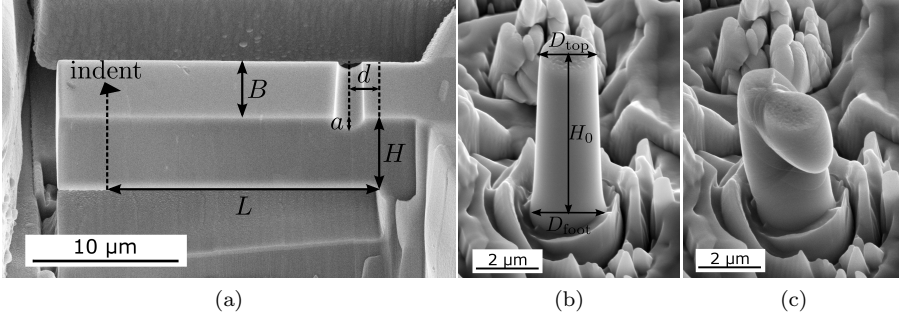


Figure 2: (a) Micro-cantilever specimen with characteristic dimensions, (b) micro-column before testing and (c) after a compression experiment to 30% nominal strain

where  $\dot{\gamma}^\alpha$  is the shear rate on the slip system  $\alpha$ ,  $\dot{\gamma}_0$  is a reference shear rate,  $\tau^\alpha$  is the resolved shear stress on a slip system,  $\tau_Y^\alpha$  is the resistance of the slip system against slip and  $n$  is the rate sensitivity exponent. In the present work the reference shear rate was  $0.001 \text{ s}^{-1}$  and the rate sensitivity exponent was taken to be 20 in order to approximate rate independence. The evolution of  $\tau_Y^\alpha$  is captured by:

$$\tau_Y^\alpha = \tau_0 + \int_0^t h(\bar{\gamma}) \left( \sum_{\beta} q_{\alpha\beta} \dot{\gamma}_{\beta} \right) dt^* \quad (2)$$

incorporating the hardening law,  $h(\bar{\gamma})$ , which depends on the accumulated plastic shear strain  $\bar{\gamma}$ .  $\tau_0$  determines the initial yield stress and  $q_{\alpha\beta}$  are the interaction coefficients that describe the influence of the hardening between different slip systems, i. e. lateral hardening. The hardening law used here is an exponential saturation hardening function:

$$h(\bar{\gamma}) = h_0 \left( 1 - \frac{\tau_0}{\tau_\infty} \right) \exp \left( -\frac{h_0 \bar{\gamma}}{\tau_\infty} \right) \quad (3)$$

with the initial hardening modulus,  $h_0$ , and the saturation hardening stress,  $\tau_\infty$ .

The aluminum alloy 2198 provides a face centered cubic structure with 12 independent slip systems. For the further investigation two interaction coefficients between these slip systems were distinguished:  $q_{\alpha\beta}^{\text{cp}}$  was used to describe the interaction between slip systems with a common slip plane (coplanar slip

systems) and  $q_{\alpha\beta}^{\text{ncp}}$  was used to describe the interaction of slip systems acting on different slip planes (non-coplanar slip systems).

#### 4. Analysis of the micro-compression data and determination of the crystal plasticity parameters

A clear definition of the yield point is required for the analysis of the micro-compression experiments in order to identify CPFEM parameters. In the context of this work, the critical resolved shear stress is associated with the point of macroscopic flow. In the case of micro-compression testing, the small specimen size and development of contact can lead to measurable plastic strains prior to yield, as defined in a continuum, macroscopic sense. This micro-plasticity must therefore be appropriately accounted for and subtracted from the data used for parameter fitting. Within this work the slope of the load-displacement curve was used as a criterion to define the onset of plastic deformation: The local slope of the load-displacement curve was calculated from linear fits of the load-displacement data within intervals of  $\pm 3$  nm around each data point. The maximum of this slope,  $S_{\text{fc}}$ , was associated with the point of full contact. The load,  $P_Y$ , and the displacement,  $h_Y$ , at yield were defined at the point where the slope of the loading curve decreased to 20% of  $S_{\text{fc}}$ . However, the surface surrounding the columns was uneven due to the anisotropic milling rates of differently oriented grains with a variation in the column height on the order of 1  $\mu\text{m}$  along the circumference of the column foot. These differences in the column height circumvent the analysis of the elastic material properties by micro-column compression experiments. However, due to the effect of taper on the stress field, the plastic deformation was restricted to the top of the columns. Hence, the displacement associated with the plastic deformation only,  $h_p$ , was determined for further analysis by subtracting the displacement associated with the maximum loading stiffness and the displacement associated with the plastic flow prior to yield from the measured displacement (see figure 3):

$$h_p(P) = h(P) - \frac{P}{S_{\text{fc}}} - \left( h_Y - \frac{P_Y}{S_{\text{fc}}} \right) \quad (4)$$

where  $h$  and  $P$  are the displacement and the load as measured from the compression experiment, respectively.

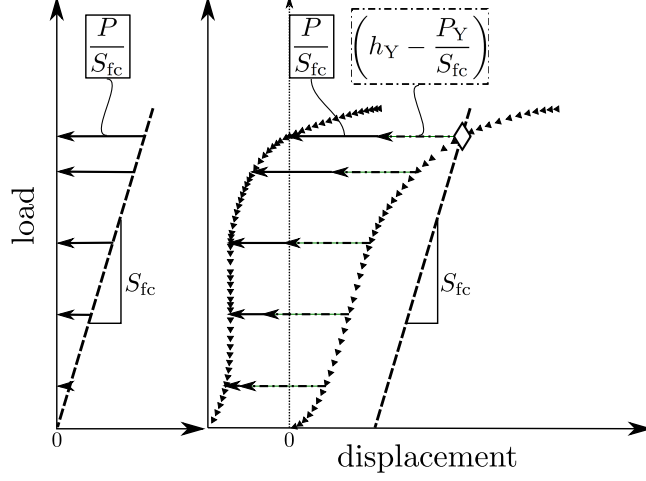


Figure 3: Determination of the displacement associated with plastic deformation only.

The geometry of the fabricated columns differs from the nominal geometry. For further comparison the load-displacement data was normalized to engineering stresses,  $\sigma$ , and engineering plastic strains,  $\varepsilon_p$ , which were defined as:

$$\sigma = \frac{P}{\bar{A}}, \quad \varepsilon_p = \frac{h_p}{H_0}, \quad (5)$$

where  $H_0$  is the initial height of the column and  $\bar{A}$  is the cross-sectional area at the center of the column:

$$\bar{A} = \frac{\pi}{4} \left( \frac{D_{\text{top}} + D_{\text{foot}}}{2} \right)^2, \quad (6)$$

with  $D_{\text{top}}$  and  $D_{\text{foot}}$  representing the diameters at the top and at the foot of the column respectively. In order to extract the material parameters the geometry of each tested column was represented as a three dimensional finite element model making use of the finite element code ABAQUS. The support was taken into account by smoothly connecting the column to a disk with a diameter of  $20 \mu\text{m}$  and a height of  $10 \mu\text{m}$ . The column and the support were modeled as a single

crystal; the orientations of the grains surrounding the column were neglected. The indenter was modeled using a displacement boundary condition on the top surface of the column not allowing for movement of the nodes contained in the top surface perpendicular to the indentation axis. Thus, the experiment was modeled assuming ideal adhesion of the indenter to the top surface of the column and no lateral compliance of the indenter.

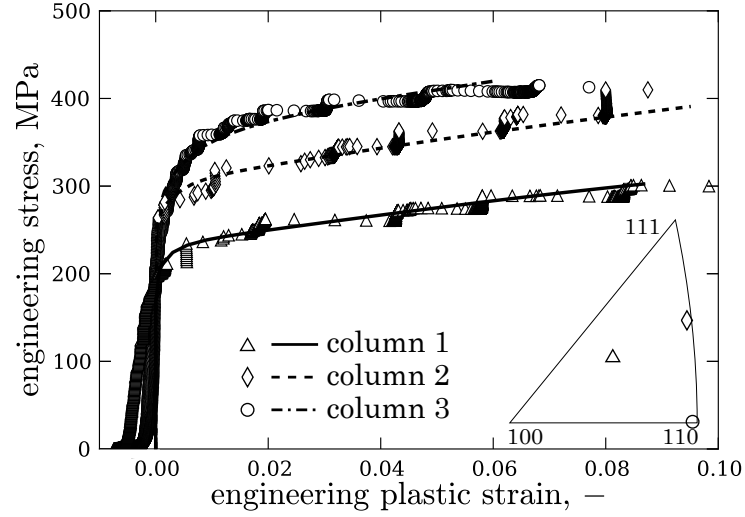
The CPFEM material model was calibrated by determining the crystal plasticity parameters such that the experimental load-displacement data of the respective columns was matched. First, the self hardening parameters,  $\tau_0$ ,  $\tau_\infty$  and  $h_0$  were adjusted to match the load-displacement data of a column oriented for single slip without the influence of lateral hardening. Then the interaction coefficient for hardening on coplanar slip systems,  $q_{\alpha\beta}^{\text{CP}}$ , was determined from the load-displacement data of a specimen where two coplanar slip systems were active. Finally, the non-coplanar interaction coefficient,  $q_{\alpha\beta}^{\text{nCP}}$ , was determined from a specimen where both coplanar and non-coplanar slip systems were active. The results are given in table 2.

$\tau_0$ , MPa	$\tau_\infty$ , MPa	$h_0$ , MPa	$q_{\alpha\beta}^{\text{CP}}, -$	$q_{\alpha\beta}^{\text{nCP}}, -$
120.0	137.0	8000.0	2.0	10.0

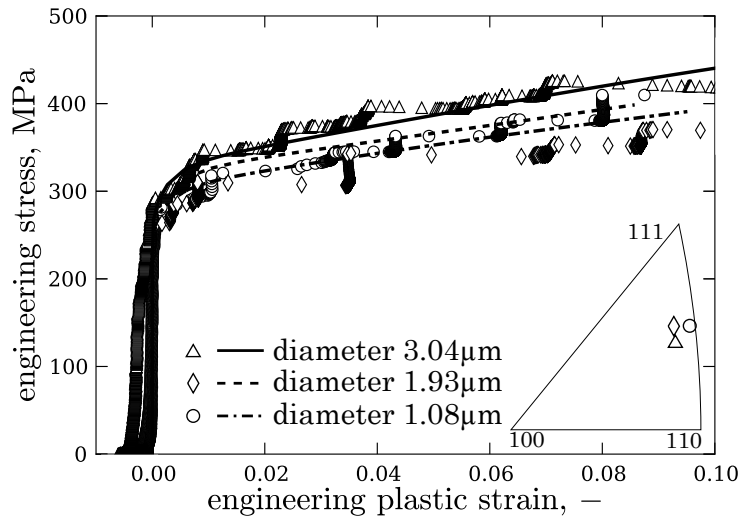
Table 2: Crystal plasticity constants determined from micro-compression experiments.

The calibrated material model was applied to columns of various orientations. An overview of the results is given in figure 4. The engineering stress vs. engineering plastic strain data extracted from the simulations was in good agreement with the experimental data of the respective columns. An exception to that were columns where a  $[1\ 1\ 1]$  crystallographic axis is approximately aligned with the compression axis. In this case the simulations overestimate the yield load on the order of 20 %.

It is worth noting that the specimen size can have a significant influence on the deformation properties when the size of the specimens reaches the characteristic dimensions of the deformation mechanisms [18, 19]. Three columns with



(a)



(b)

Figure 4: (a) Experimental data (markers) and corresponding simulation data (lines) from micro-compression experiments of three micro-columns with varying orientations. (b) Experimental data (markers) and corresponding simulation data (lines) from micro-compression experiments of single three micro-columns with varying diameters.

sizes of 1  $\mu\text{m}$ , 2  $\mu\text{m}$  and 3  $\mu\text{m}$  and with approximately identical crystallographic orientations were tested, in order to investigate possible size effects. Figure 4(b) shows the engineering stress vs. engineering plastic strain data for these experiments together with the respective simulations. No systematic differences are found between the datasets indicating that the specimen size does not significantly influence the plastic deformation properties within the given range of specimen dimensions. The absence of a size effect is not unexpected. Due to the alloying content and the thermo-mechanical treatment of the material the microstructural length-scale controlling the stress-strain behavior is expected to be much smaller than the geometric length-scale associated with the diameter of the column, thereby mitigating the size effect.

## 5. Application of the crystal plasticity model in a cantilever specimen

Finite element models for each cantilever were created with the bending length,  $L$ , the width,  $B$ , the height,  $H$ , the position,  $d$ , and the depth,  $a$ , of the notch (see figure 5(a)). Additionally, the support was modeled explicitly. The crystallographic orientations of the grains adjacent to the notch were provided for both types of cantilevers as given in figure 5(b). The orientation of the remaining parts of the cantilever was chosen such that a  $[1\ 1\ 0]$  crystallographic axis was aligned with the cantilever axis. A continuous displacement was assured at the grain boundaries. This is reasonable since the fracture experiments in [9] showed that no damage is induced at the grain boundaries prior to complete fracture. The deflection of the cantilever within the simulation was displacement controlled at the displacement rate of 5 nm/s. The elastic modulus of the material at the loading point was given as  $10^6$  GPa in order to prevent severe distortions of the elements. Such a high contact stiffness negated the need for any indentation correction in the finite element analysis; the displacement in the simulation corresponds to the cantilever deflection. Moreover, the lateral stiffness of the indenter was required for the model since the loading point is significantly deviated in the lateral direction during the bending experiment. Hence, two spring elements at the loading point were used to create this

additional constraint. The spring stiffness was chosen according to the calibration data of the lateral stiffness of the nanoindenter, which is on the order of 10 kN/m.

The effect of the crystal orientation on the deformation behavior of the cantilevers can be estimated by two simulations of single crystalline cantilevers with the same geometry and particular crystallographic orientations along the cantilever axis. Since the normal stress along the cantilever axis is dominating the Schmid factors for loading in the direction of the cantilever axis are decisive. The lowest Schmid factor for the FCC crystals is achieved when the  $[111]$  direction is aligned with the cantilever axis; the highest resistance against plastic deformation can be expected in this case. The maximum Schmid factor is achieved for a single slip orientation aligned with the cantilever axis, leading to the lowest resistance. This effect is illustrated in figure 6. An increase of the load levels for plastic deformation on the order of 30 % was found between these distinct orientations. These simulations provide the limits for the effect of the crystal orientation on the load-displacement response of a cantilever and demonstrate the importance of using anisotropic plastic constitutive models for the analysis of the cantilever bending/fracture experiments.

In figure 7(a) the experimental load-displacement response of one cantilever with a grain boundary under the notch and one cantilever with the notch within a single grain is compared to the load-displacement data extracted from the simulation of the respective cantilever. While the beginning of the plastic deformation is well predicted for both cantilevers, the simulations overestimate the hardening of the material, thus, the load after yield. The deviation of the load between experimental and simulated data after a significant amount of plastic deformation can be estimated with the displacement at fracture of the cantilever with a grain boundary under the notch is chosen as a reference point. In both cases the load level is overestimated approximately by 15 %. These deviations are likely related to the different boundary conditions associated with the grain boundaries in the cantilever. The presence of a grain boundary under the notch results in more complex boundary conditions for the plastic deformation; the

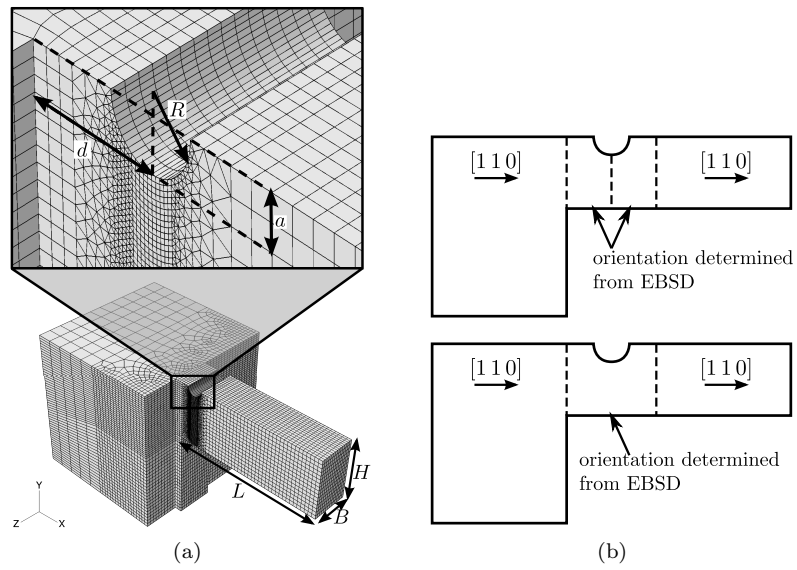


Figure 5: (a) Finite element model of a cantilever and (b) orientations within the cantilever.

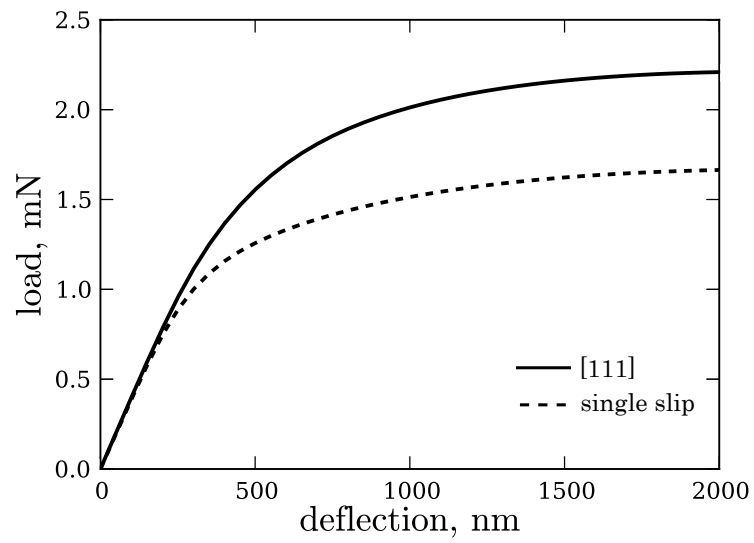


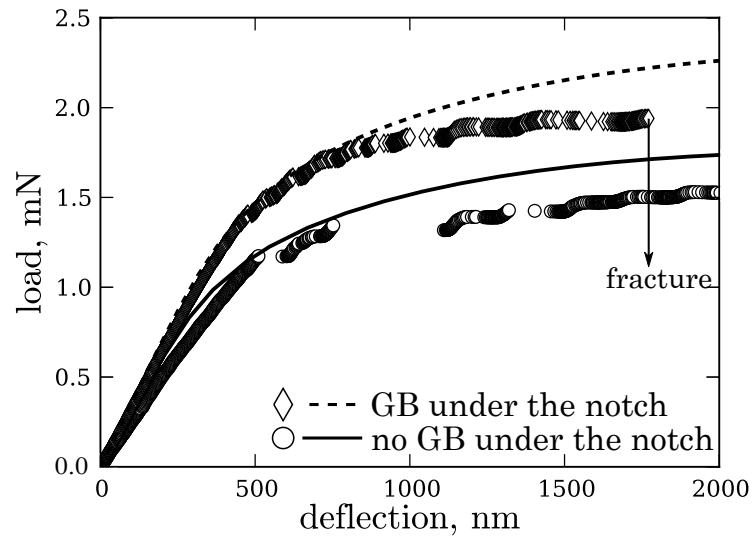
Figure 6: Effect of the orientation of the crystals along the cantilever axis on the deformation of two cantilevers with the nominal dimensions  $20 \mu\text{m} : 5 \mu\text{m} : 8 \mu\text{m}$  (length : width : height).

transmission of slip through the grain boundary [36, 37]. The method presented here, thus, enables an analysis of the boundary conditions that are imposed by specific grain boundaries in technological alloys. Figure 7(b) depicts the load-displacement data after the normalization according to [9]. Here, the difference in the normalized load levels between the cantilevers at the beginning of the plastic deformation are related to differences in the crystallographic orientation of the grains.

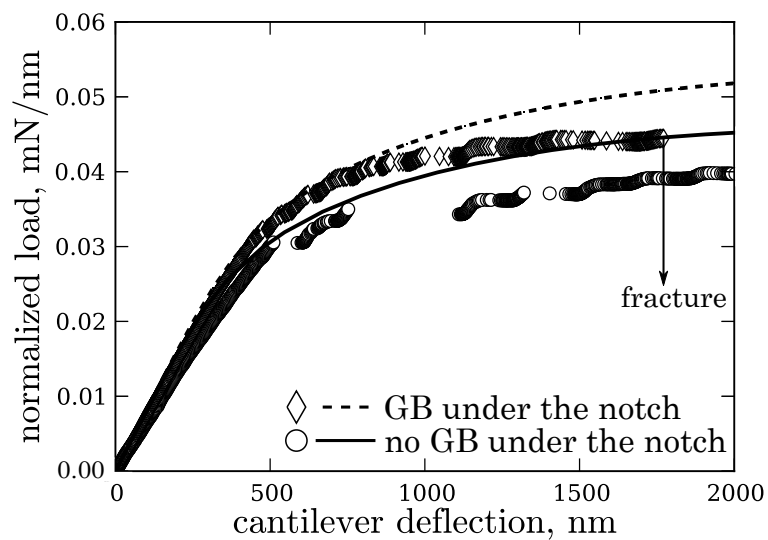
In order to further validate the applicability of the crystal plasticity model, local measurements in the vicinity of the notch are required. Therefore, the displacement field under the notch was determined for the cantilever with the speckle pattern. The image of the deformed cantilever was recorded at a constant load and the displacement field was determined by DIC (see figure 8(a)). The determination of the strains from the measured displacements is circumvented by the scatter in the displacement measurement which is on the order of 10 nm. This scatter is likely related to the size of the Pt-dots of the speckle pattern. Further refinement of the speckle pattern is expected to allow for the determination of the strain fields from the experiment. Importantly, the displacement field predicted by the simulation at the corresponding load approximates both the shape and the magnitude of the displacement field measured in the experiment, as shown in figure 8(b). Differences between the simulation and the experimental data are found in the vicinity of the notch but cannot be further evaluated due to the scatter.

## **6. Fracture Parameters of an Individual Grain Boundary**

Since the plastic deformation of the grains is captured by the CPFEM, the simulations may be used to determine the fracture properties of an individual grain boundary. Within finite element simulations, cohesive zone modeling is capable to model the initiation and propagation of cracks independently of the microscopic mechanism. Therefore, the extension of the finite element model given in figure 5(a) by a cohesive zone, as shown in figure 9, provides access to the fracture properties of an individual grain boundary. The grain boundary



(a)



(b)

Figure 7: (a) Experimental load-displacement data (markers) from micro-cantilever bending experiments of two cantilevers with and without a grain boundary at the location of the notch. The lines represent the respective simulation data. (b) The dataset normalized according to the method presented in [9].

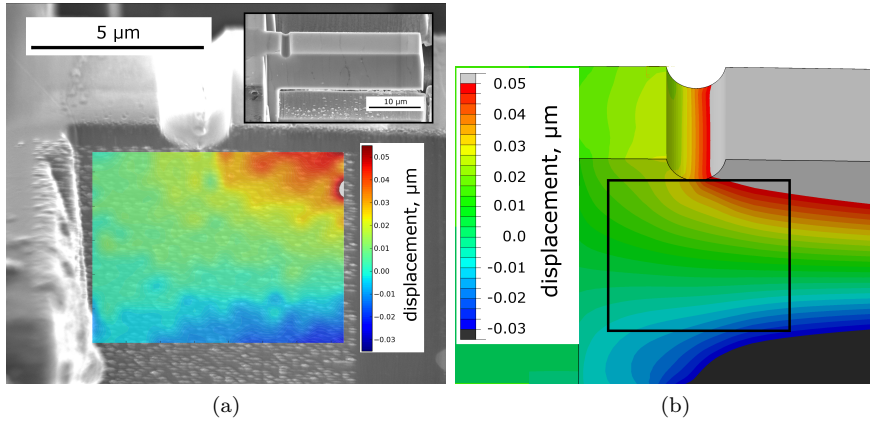


Figure 8: Displacement field at the notch of a cantilever (a) measured by digital image correlation and (b) extracted from the corresponding FEM simulation at the same load. (color online)

was modeled as an infinitesimal thin interface perpendicular to the cantilever axis using the ABAQUS COH3D8 elements [38]. Since the normal stress along the cantilever axis dominates the stress field for the chosen cantilever geometry, the analysis of the fracture was restricted to the normal fracture mode. The analysis of the influence of the shear components on the interface is beyond the scope of this paper. The constitutive model for the cohesive material was a bilinear traction-separation-law according to:

$$t = \begin{cases} K\delta & \text{for } \delta \leq \delta_i \\ (1 - D) \cdot K\delta & \text{for } \delta > \delta_i \end{cases} \quad (7)$$

where  $t$  is the normal traction of the element and  $\delta$  is the normal separation of the element.  $\delta_i$  is the displacement at damage initiation and  $D$  is a damage variable with  $D = 0$  represents the undamaged state and  $D = 1$  corresponds to complete fracture. Damage is initiated when the normal traction exceeds the initiation stress denoted by  $t_i$ .

The damage variable for linear damage evolution is expressed as:

$$D = \frac{\delta_f (\delta_{\max} - \delta_i)}{\delta_{\max} (\delta_f - \delta_i)} \quad (8)$$

with  $\delta_{\max}$  denoting the maximum value of the displacement attained during the loading history and  $\delta_f$  is the separation of the element in the fully damaged state. Finally, the separation at the fully damaged state,  $\delta_f$ , is coupled to the fracture energy,  $G_f$  by:

$$G_f = \frac{1}{2} \delta_f t_i . \quad (9)$$

By choosing a relatively high cohesive stiffness,  $K$ , of 750 GPa the elastic de-

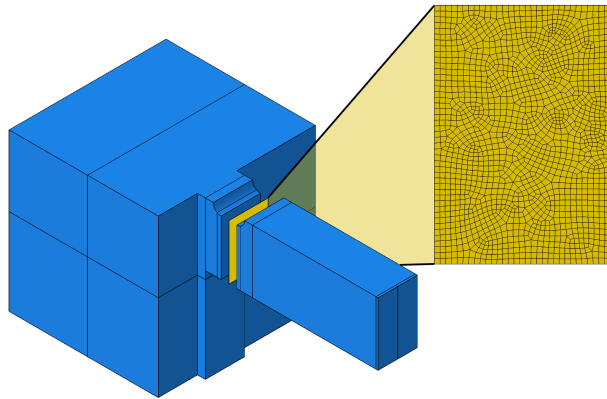


Figure 9: Incorporation of the cohesive zone in the FE-model of the cantilever.

formation of the interface becomes negligible compared to the elasto-plastic deformation of the adjacent grains. The constant elastic cantilever stiffness during the experiment indicates that no crack propagation is found prior to complete fracture of the grain boundary. This is supported by the fact that no crack is visible during an *in situ* experiment prior to complete fracture. In order to model such brittle grain boundaries a relatively small value of  $5 \text{ J/m}^2$  was assumed as a constant value for the fracture energy. Similar material combinations show values between  $0.3 \text{ J/m}^2$  and  $3.0 \text{ J/m}^2$  [39]. The higher value chosen in this work is motivated by the numerical stability of the simulations. With these assumptions, only the initiation stress,  $t_i$ , remains to be determined as a parameter for the fracture of a grain boundary.

The determination of the initiation stress can be realized using the load-displacement response of a cantilever as shown in figure 7(a). Multiple sim-

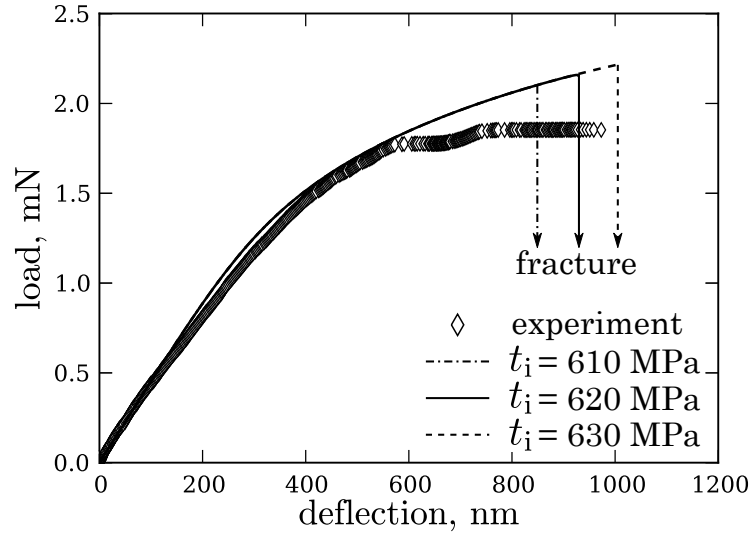
ulations with varying values of the initiation stress were carried out for two cantilevers which are denoted cantilever I and cantilever II. The geometry of both cantilevers is given in table 3 and the load-displacement data is shown in figure 10. For cantilever I, which showed less plastic deformation prior to fracture than cantilever II, an initiation stress on the order of  $620 \text{ MPa} \pm 10 \text{ MPa}$  approximates the displacement at failure. The initiation stress for fracture of cantilever II was on the order of  $600 \text{ MPa} \pm 10 \text{ MPa}$ . Further simulations showed that the influence of  $t_i$  on the displacement of fracture is more pronounced than the influence of a variation in the fracture energy.

The grain boundaries fractured in both cantilevers are high angle grain boundaries as determined from the EBSD measurements given in table 4. Both grain boundaries were separated with a similar initiation stress while there are remarkable differences concerning the extend of plastic deformation prior to fracture. This underscores the importance of a suitable incorporation of the plastic deformation of the grains in the analysis of the fracture of individual grain boundaries.

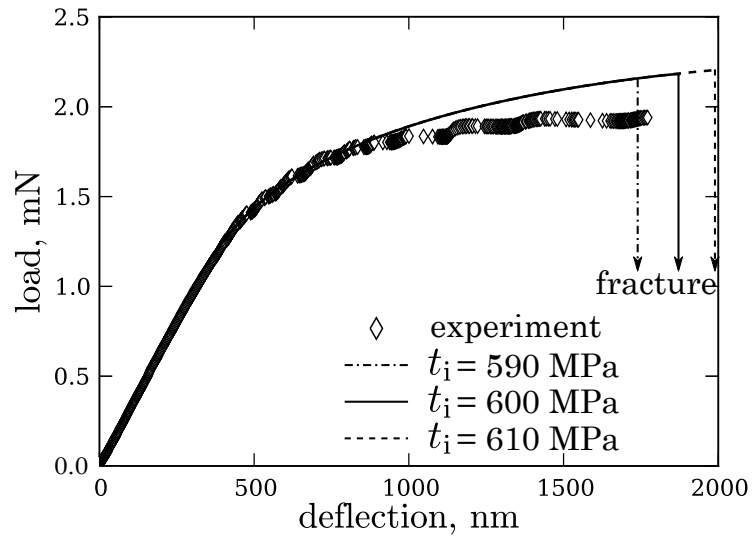
It is worth noting that the stress field at the grain boundary is not expected to be reproduced exactly by the simulation. The stress field at a grain boundary is influenced by the boundary conditions for the transmission of slip as pointed out in section 5. Moreover, the grain boundary itself may have facets and particles or grain boundary precipitates which alter the stress field in the grain boundary plane. The model with idealized geometry and the continuous displacement boundary condition, thus, provides the possibility to investigate the influence of these effects on the fracture strength of a grain boundary.

## 7. Conclusions

The fracture properties of individual brittle grain boundaries in a ductile technological aluminum alloy were determined using a combination of CPFEM simulations and micro-mechanical experiments. The grain boundary fracture experiments were conducted using micro-cantilever bending specimens. In order



(a)



(b)

Figure 10: Load-displacement response for bending/fracture experiments of cantilever I and II together with the FE-simulations with varying initiation stress.

cantilever	$H, \mu\text{m}$	$L, \mu\text{m}$	$B, \mu\text{m}$	$d, \mu\text{m}$	$a, \mu\text{m}$
I	8.70	21.64	6.13	3.13	1.02
II	9.43	26.70	7.02	4.55	1.13

Table 3: Geometry of the cantilevers I and II.  $H$  is the cantilever height,  $L$  is the cantilever length,  $B$  is the cantilever width,  $d$  is the position of the notch center and  $a$  is the depth of the notch.

cantilever	grain	$\phi_1$	$\Phi$	$\phi_2$	$\theta$
I	support	148.9°	62.1°	46.2°	47.5°
	free	152.4°	112.6°	55.9°	
II	support	209.4°	108.3°	218.3°	51.5°
	free	87.0°	92.2°	0.3°	

Table 4: Orientations of the grains under the notch for cantilevers I and II in terms of Eulerian angles ( $\phi_1, \Phi, \phi_2$ ) in the Bunge notation. The label “support” denotes the orientations of the grains close to the supported end, the label “free” denotes the orientations of the grains close to the free end of the cantilever.  $\theta$  is the misorientation angle of the grain boundary.

to access the anisotropic plastic deformation properties of the single grains independently from the fracture experiments, CPFEM model parameters were identified. Since no macroscopic single crystals of this specific temper are available, micro-compression experiments on single crystalline micro-columns were used to identify the model parameters. It was shown that the measured properties of the single crystals were not influenced by the size of the specimens in the accessible range. The material model was validated for the use in micro-cantilever specimens; the CPFEM parameters identified from micro-compression experiments allow the prediction of the plastic deformation of the notched micro-cantilever specimens in a bending/fracture experiment. The independent determination of the CPFEM parameters through micro-compression experiments is particularly important for technological alloys where macroscopic single crystals are not available.

Differences between the prediction and the experimental data from the micro-cantilever bending experiment are likely related to the different deformation

mode of the bending specimens and the presence of a grain boundary which is an obstacle to plastic slip. Thus, such experiments offer the possibility to investigate the influence of the grain boundary structure on the plastic deformation. The fracture properties of an individual grain boundary can be determined in terms of a traction-separation-law associated with a cohesive zone. The idealized model with a perfectly plane grain boundary provides the possibility to investigate the influence of the structure of the grain boundary on the initiation stress for fracture. For aluminum-lithium alloys, this can be the presence of precipitates at the grain boundaries, which is expected to increase the sensitivity to intergranular fracture. Additionally, the dependence of the fracture parameters on the orientation of a grain boundary can be investigated with this method. Moreover, the method allows to investigate the influence of the misorientation of grain boundaries on their sensitivity towards liquid metal embrittlement.

The combination of microscopic fracture experiments with the CPFEM and cohesive zones allows the analysis of the deformation behavior in the vicinity of a grain boundary in ductile metals and the determination of fracture properties of such grain boundaries depending on their structure.

## References

- [1] D. Di Maio, S. Roberts, Rapid communications: Measuring fracture toughness of coatings using focused-ion-beam-machined microbeams, *Journal of Materials Research* 20 (2005) 299–302.
- [2] C. Motz, R. Pippan, T. Schöberl, Mechanical properties of micro-sized copper bending beams machined by the focused ion beam technique, *Acta Materialia* 53 (2005) 4269–4279.
- [3] T. Halford, K. Takashima, Y. Higo, P. Bowen, Fracture test of micro-sized TiAl specimens, *Fatigue and Fracture of Engineering Materials and Structures* 28 (2005) 695–701.
- [4] T. Klüsner, S. Wurster, P. Supancic, R. Ebner, M. Jenko, J. Glätzle, A. Püschel, R. Pippan, Effect of specimen size on the tensile strength of WC–Co hard metal, *Acta Materialia* 59 (2011) 4244–4252.
- [5] H. Hirakata, Y. Takahashi, V. Truong, T. Kitamura, Role of plasticity on interface crack initiation from a free edge and propagation in a nano-component, *International Journal of Fracture* 145 (2007) 261–271.
- [6] K. Matoy, H. Schönherr, T. Detzel, T. Schöberl, R. Pippan, C. Motz, G. Dehm, A comparative micro-cantilever study of the mechanical behavior of silicon based passivation films, *Thin Solid Films* 518 (2009) 247–256.
- [7] D. Armstrong, M. Rogers, S. Roberts, Micromechanical testing of stress corrosion cracking of individual grain boundaries, *Scripta Materialia* 61 (2009) 741–743.
- [8] D. Armstrong, A. Wilkinson, S. Roberts, Micro-mechanical measurements of fracture toughness of bismuth embrittled copper grain boundaries, *Philosophical Magazine Letters* 91 (2011) 394–400.
- [9] D. Kupka, E. Lilleodden, Mechanical testing of solid-solid interfaces at the microscale, *Experimental Mechanics* 52 (2012) 649–658.

- [10] A. Vasudevan, R. Doherty, Grain boundary ductile fracture in precipitation hardened aluminum alloys, *Acta Metallurgica* 35 (1987) 1193–1219.
- [11] S. Suresh, A. Vasudevan, M. Tosten, P. Howell, Microscopic and macroscopic aspects of fracture in lithium containing aluminum alloys, *Acta Metallurgica* 35 (1987) 25–46.
- [12] F. Iqbal, J. Ast, M. Göken, K. Durst, In situ micro-cantilever tests to study fracture properties of NiAl single crystals, *Acta Materialia* 60 (2012) 1193–1200.
- [13] S. Wurster, C. Motz, R. Pippan, Characterization of the fracture toughness of micro-sized tungsten single crystal notched specimens, *Philosophical Magazine* 92 (2012) 1803–1825.
- [14] F. Roters, P. Eisenlohr, L. Hantcherli, D. Tjahjanto, T. Bieler, D. Raabe, Overview of constitutive laws, kinematics, homogenization and multiscale methods in crystal plasticity finite-element modeling: Theory, experiments, applications, *Acta Materialia* 58 (2010) 1152–1211.
- [15] D. Raabe, F. Roters, Using texture components in crystal plasticity finite element simulations, *International Journal of Plasticity* 20 (2004) 339–361.
- [16] Z. Zhao, W. Mao, F. Roters, D. Raabe, A texture optimization study for minimum earing in aluminium by use of a texture component crystal plasticity finite element method, *Acta Materialia* 52 (2004) 1003–1012.
- [17] B. Klusemann, B. Svendsen, H. Vehoff, Investigation of the deformation behavior of fe-3%si sheet metal with large grains via crystal plasticity and finite-element modeling, *Computational Materials Science* 52 (2012) 25–32.
- [18] M. Uchic, D. Dimiduk, J. Florando, W. Nix, Sample dimensions influence strength and crystal plasticity, *Science* 305 (2004) 986–989.
- [19] C. Volkert, E. Lilleodden, Size effects in the deformation of sub-micron Au columns, *Philosophical Magazine* 86 (2006) 5567–5579.

- [20] M. Uchic, D. Dimiduk, R. Wheeler, P. Shade, H. Fraser, Application of micro-sample testing to study fundamental aspects of plastic flow, *Scripta Materialia* 54 (2006) 759–764.
- [21] J. Greer, C. Weinberger, W. Cai, Comparing the strength of f.c.c. and b.c.c. sub-micrometer pillars: Compression experiments and dislocation dynamics simulations, *Materials Science and Engineering A493* (2008) 21–25.
- [22] D. Raabe, D. Ma, F. Roters, Effects of initial orientation, sample geometry and friction on anisotropy and crystallographic orientation changes in single crystal microcompression deformation: A crystal plasticity finite element study, *Acta Materialia* 55 (2007) 4567–4583.
- [23] R. Soler, J. Molina-Aldareguia, J. Segurado, J. Llorca, R. Merino, V. Orera, Micropillar compression of LiF [111] single crystals: Effect of size, ion irradiation and misorientation, *International Journal of Plasticity* 36 (2012) 50–63.
- [24] J. Gong, A. Wilkinson, Anisotropy in the plastic flow properties of single-crystal  $\alpha$  titanium determined from micro-cantilever beams, *Acta Materialia* 57 (2009) 5693–5705.
- [25] F. Dunne, D. Rugg, A. Walker, Lengthscale-dependent, elastically anisotropic, physically-based hcp crystal plasticity: Application to cold-dwell fatigue in ti alloys, *International Journal of Plasticity* 23 (2007) 1061–1083.
- [26] P. Cavaliere, A. de Santis, Effect of anisotropy on fatigue properties of AA2198 Al-Li plates joined by friction stir welding, *Metallurgical Science and Technology* 26 (2008) 21–30.
- [27] H. Bruck, S. McNeill, M. Sutton, W. Peters, Digital image correlation using newton-raphson method of partial differential correction, *Experimental Mechanics* 29 (1989) 261–267.

- [28] T. Chu, W. Ranson, M. Sutton, W. Peters, Applications of digital-image-correlation techniques to experimental mechanics, *Experimental Mechanics* 25 (1985) 232–244.
- [29] Z. Wang, P. Vo, A free 2d and 3d digital image correlation (DIC) moire software, Available at <http://www.opticist.org/node/73>.  
URL <http://www.opticist.org>
- [30] D. Kiener, C. Motz, T. Schöberl, M. Jenko, G. Dehm, Determination of mechanical properties of copper at the micron scale, *Advanced Engineering Materials* 8 (2006) 1119–1125.
- [31] E. Lilleodden, Microcompression study of Mg (0001) single crystal, *Scripta Materialia* 62 (2010) 532–535.
- [32] D. Peirce, R. Asaro, N. A., An analysis of nonuniform and localized deformation in ductile single crystals, *Acta Metallurgica* 30 (1982) 1087–1119.
- [33] R. Asaro, Crystal plasticity, *J. Appl. Mech.-Trans.* 50 (1983) 921–934.
- [34] Y. Huang, A user material subroutine incorporating single crystal plasticity in the abaqus finite element program, technical report mech 178, Tech. rep., Harvard University, Division of applied sciences (1991).
- [35] S. Graff, Micromechanical modeling of deformation in hcp metals, Ph.D. thesis, Technische Universität Berlin, Germany (2007).
- [36] L. Evers, W. Brekelmans, M. Geers, Scale dependent crystal plasticity framework with dislocation density and grain boundary effects, *International Journal of Solids and Structures* 41 (2004) 5209–5230.
- [37] A. Ma, F. Roters, D. Raabe, On the consideration of interactions between dislocations and grain boundaries in crystal plasticity finite element modeling – Theory, experiments and simulations, *Acta Materialia* 54 (2006) 2181–2194.

- [38] ABAQUS Analysis User's Manual (version 6.11), 31.5 Cohesive Elements, Dassault Systèmes, 2011.
- [39] J. Kargol, D. Albright, The effect of relative crystal orientation on the liquid metal induced grain boundary fracture of aluminum bicrystals, Metallurgical Transactions A 8 (1977) 27–34.